PHYSICAL REVIEW D VOLUME 43, NUMBER 1 1 JANUARY 1991

Precision measurement of the pion mass difference $m_{\pi^-} - m_{\pi^0}$

J. F. Crawford, M. Daum, R. Frosch, B. Jost,* and P.-R. Kettle
Paul Scherrer Institute, CH-5232 Villigen-PSI, Switzerland

R. M. Marshall, B. K. Wright, and K. O. H. Ziock
Physics Department, University of Virginia, Charlottesville, Virginia 22901

(Received 13 August 1990; revised manuscript received 26 November 1990)

We have studied the time-of-flight spectra of neutrons produced by the charge-exchange reaction $\pi^- p \rightarrow \pi^0 n$ of $\pi^- p$ atoms in liquid hydrogen, at flight distances up to 18.1 m. We have found the neutron velocity for $\pi^- p$ atoms at rest to be $0.894\,266 \pm 0.000\,063$ cm/ns, corresponding to a pion mass difference $m_{\pi^-} - m_{\pi^0} = 4.593\,64 \pm 0.000\,48$ MeV. As an additional result, we have observed a broadening of the neutron time-of-flight peak with increasing flight distance, which implies that the kinetic-energy distribution of the $\pi^- p$ atoms just before the charge-exchange reaction has one component extending up to ~ 1 eV and another component extending up to ~ 70 eV; each component contains about half of the $\pi^- p$ atoms.

I. INTRODUCTION

The mass m_{π^0} of the neutral pion and the mass difference $D_\pi \equiv m_{\pi^-} - m_{\pi^0}$ are important constants of particle physics; e.g., a precise value of D_π is needed for the comparison of the rate $\Gamma_{\pi\beta}$ of pion β decay $\pi^\pm \rightarrow \pi^0 e^\pm \nu$ with theoretical predictions. In the two decades from 1966 to 1985 no improved measurements of the mass difference D_π were made, whereas in the same period the uncertainty in the charged-pion mass m_{π^-} was reduced by a factor of about 15. As a consequence, the uncertainty in the 1986 world average of m_{π^-}, $\Delta m_{\pi^-} = 1.0$ keV,[1] was considerably smaller than $\Delta m_{\pi^0} \approx \Delta D_\pi = 3.7$ keV.

In the present measurement of D_π, which was briefly described in a previous publication,[2] negative pions are stopped in a liquid-hydrogen target, to form pionic hydrogen atoms. A fraction $R \approx R_P/(R_P+1) \approx 0.6$ of these $\pi^- p$ atoms, where R_P is the Panofsky ratio, undergo the charge-exchange reaction

$$\pi^- p \rightarrow \pi^0 n \ , \tag{1}$$

whereas almost all of the remaining 40 percent of the $\pi^- p$ atoms undergo radiative capture:

$$\pi^- p \rightarrow \gamma n \ . \tag{2}$$

The mass difference D_π is derived from time-of-flight (TOF) distributions of neutrons from reaction (1), measured at flight distances of 3.2, 7.9, and 18.1 m. Since the $\pi^- p$ atoms are nearly at rest, these neutrons generate a TOF peak corresponding to their velocity of ~ 0.894 cm/ns.

As an additional result, we have observed a broadening of the neutron TOF peak with increasing flight distance, which contains information on the kinetic energy distribution $f(T_{\pi p})$ of the $\pi^- p$ atoms immediately before reaction (1). The distribution $f(T_{\pi p})$ can be used to test models of the cross sections of the various processes that can occur during the deexcitation of exotic hydrogen atoms. One of these processes is Coulomb deexcitation[3]

$$(\pi^- p)_n p \rightarrow (\pi^- p)_{n'} p \tag{3}$$

of the $\pi^- p$ atom in the electric field of a proton of the surrounding liquid hydrogen. In this process the kinetic energy of the $\pi^- p$ atom is increased to typically about half of the deexcitation energy associated with the initial and final principal quantum numbers n and n'. A second process, elastic scattering of a nonthermalized $\pi^- p$ atom by normal hydrogen molecules, reduces the kinetic energy $T_{\pi p}$; and a third process, Auger deexcitation involving an electron of the liquid hydrogen,

$$(\pi^- p)_n e^- \rightarrow (\pi^- p)_{n'} e^- \ , \tag{4}$$

leaves $T_{\pi p}$ almost unchanged. Because of the very different effects of the various processes on the kinetic energy of the $\pi^- p$ atom, the function $f(T_{\pi p})$ depends strongly on their cross sections.

II. KINEMATICS

A. Pionic hydrogen atoms at rest

If the $\pi^- p$ atoms are assumed to be at rest before reaction (1), energy and momentum conservation lead to the following equation for the mass difference $D_\pi \equiv m_{\pi^-} - m_{\pi^0}$:

$$D_\pi = m_{\pi^-} - [(m_{\pi^-} - D_N - E_B)^2 - 2(\gamma_{\rm nr} - 1)(m_p + D_N)(m_{\pi^-} + m_p - E_B)]^{1/2} . \tag{5}$$

Here $D_N \equiv m_n - m_p$ is the nucleon mass difference and E_B is the binding energy of the $\pi^- p$ atom just before re-

©1991 The American Physical Society

action (1); the rest mass of the $\pi^- p$ atom is $m_{\pi p} = m_{\pi^-} + m_p - E_B$; $\gamma_{\rm nr} \equiv (1+\beta_{\rm nr}^2)^{-1/2}$ is the usual function of neutron velocity $v_{\rm nr} = c\beta_{\rm nr}$ for $\pi^- p$ atoms at rest; we set $c = 1$, except where the units are given explicitly.

From Eq. (5), it follows that the experimental uncertainty in the mass difference D_π contains five contributions due to the uncertainties in $\beta_{\rm nr}$, m_{π^-}, m_p, D_N, and E_B. The contribution from the quantity $\beta_{\rm nr}$, measured in the present experiment, is determined by differentiation of Eq. (5):

$$(\Delta D_\pi)_{\beta_{\rm nr}} = |\partial D_\pi / \partial \beta_{\rm nr}| \Delta\beta_{\rm nr} = (m_{\pi p} m_n \beta_{\rm nr} \gamma_{\rm nr}^3 / m_{\pi^0}) \Delta\beta_{\rm nr}$$

$$= (224 \text{ MeV}) \Delta\beta_{\rm nr} . \qquad (6)$$

The corresponding relative uncertainty of D_π is of the same order as that of $\beta_{\rm nr}$:

$$(\Delta D_\pi)_{\beta_{\rm nr}} / D_\pi = 1.46 \Delta\beta_{\rm nr} / \beta_{\rm nr} . \qquad (7)$$

The remaining four contributions to the uncertainty ΔD_π are similarly found by differentiations of Eq. (5):

$$(\Delta D_\pi)_{m_{\pi^-}} = 0.021 \Delta m_{\pi^-} , \qquad (8)$$

$$(\Delta D_\pi)_{m_p} = 0.0067 \Delta m_p , \qquad (9)$$

$$(\Delta D_\pi)_{D_N} = 1.03 \Delta D_N , \qquad (10)$$

$$(\Delta D_\pi)_{E_B} = 1.02 \Delta E_B . \qquad (11)$$

If the uncertainties in m_{π^-}, m_p, and D_N given in Ref. 4 are inserted into Eqs. (8)–(10), the resulting contributions to ΔD_π are ~0.02 keV and can therefore be neglected compared to the total D_π uncertainty of ~0.5 keV.

The last contribution to ΔD_π, related to the binding energy E_B of the $\pi^- p$ atom, can be derived from the uncertainties in the calculations of the nuclear capture probabilities $P(n)$, where n is the principal quantum number of the $\pi^- p$ atom just before nuclear capture. This capture in liquid hydrogen has been calculated by Leon and Bethe[5] to occur predominantly from atomic states with $n = 3$ or 4, whereas capture from the ground state ($n = 1$) is known, from the absence of a significant K x-ray yield in the experimental data of Budick *et al.*,[6] to occur at most in a few percent of all cases.

Estimates of the capture probabilities $P(n)$ and their uncertainties are listed in Table I. The probability $P(1)$ and the uncertainty $\Delta P(1)$ given in the table are estimated from the theoretical K x-ray yields calculated by Borie and Leon.[7] The probabilities $P(n)$ for $n > 1$ (but not their uncertainties) are the results of the calculation by Leon and Bethe.[5] We have made calculations similar to those of Refs. 5 and 7, but including Coulomb deexcitation, for which cross sections were estimated from the calculation of Men'shikov.[3,8] The uncertainties $\Delta P(n)$ for $n > 1$ quoted in Table I were estimated from the differences between our results and those of Ref. 5.

TABLE I. Estimates of the probabilities $P(n)$ of the principal quantum number n of $\pi^- p$ atoms in liquid hydrogen just before the capture reaction (1) or (2). $E_B(n)$ is the $\pi^- p$ atomic binding energy in the state n.

n	$P(n)$	$E_B(n)$ (eV)
1	0.03±0.02	3235
2	0.04±0.04	809
3	0.39±0.10	359
4	0.44±0.10	202
5	0.09±0.03	129
6	0.01±0.01	90

From Table I we conclude that the mean binding energy $\overline{E_B}$ of the $\pi^- p$ atoms just before reaction (1) or (2) is

$$\overline{E_B} = 0.37 \pm 0.08 \text{ keV} . \qquad (12)$$

This uncertainty in $\overline{E_B}$, inserted into Eq. (11), leads to the contribution $(\Delta D_\pi)_{E_B} = 0.08$ keV, which is only one sixth of our total uncertainty in D_π; see Sec. V.

B. Pionic hydrogen atoms in motion

1. Determination of the neutron velocity β_{nr}

If the $\pi^- p$ atoms are assumed to move with isotropically distributed velocities $\boldsymbol{\beta}_{\pi p}$ of constant absolute magnitude $\beta_{\pi p} \equiv (1-\gamma_{\pi p}^{-2})^{1/2}$ just before reaction (1), the neutron TOF distribution dN/dt_n for a given neutron flight path l is[9]

$$dN/dt_n = l^2 / [2\beta_{\pi p} \gamma_{\pi p} \beta_{\rm nr} \gamma_{\rm nr} (t_n^2 - l^2)^{3/2}] , \qquad (13)$$

with the flight time limits

$$\begin{aligned} t_n(\min) &= l(1+\beta_{\pi p}\beta_{\rm nr})/(\beta_{\rm nr}+\beta_{\pi p}) , \\ t_n(\max) &= l(1-\beta_{\pi p}\beta_{\rm nr})/(\beta_{\rm nr}-\beta_{\pi p}) . \end{aligned} \qquad (14)$$

The quantities $\beta_{\rm nr}$ and $\gamma_{\rm nr}$ are defined in Sec. II A.

The time distribution defined by Eqs. (13) and (14) has a mean

$$\overline{t_n} = \int_{t_n(\min)}^{t_n(\max)} (dN/dt_n) t_n dt_n = l/\beta_{\rm nr} = t_{\rm nr} ; \qquad (15)$$

i.e., the mean flight time is exactly equal to the flight time $t_{\rm nr}$ for $\pi^- p$ atoms at rest. This conclusion is valid also if the velocity $\beta_{\pi p}$ just before reaction (1) differs from one $\pi^- p$ atom to the next.

2. Determination of the kinetic-energy distribution $f(T_\pi p)$

For the determination of the distribution $f(T_{\pi p})$, where $T_{\pi p} \approx m_{\pi p} \beta_{\pi p}^2 / 2$ is the kinetic energy of the $\pi^- p$ atom just before reaction (1), nonrelativistic approximations can be used. In our experiment we have $\beta_{\rm nr} \approx 0.03$ and $\beta_{\pi p} < 4 \times 10^{-4}$ (kinetic energy $T_{\pi p} < 100$ eV). Under these conditions, i.e., if $\beta_{\pi p} \ll \beta_{\rm nr} \ll 1$, the time spectrum of Eqs. (13) and (14) can be well approximated by a flat spectrum

$$dN/dt_n=\beta_{\rm nr}^2/(2\beta_{\pi p}l)\ , \qquad (16)$$

with the limits

$$t_n(\min)=(l/\beta_{\rm nr})(1-\beta_{\pi p}/\beta_{\rm nr})\ ,$$
$$t_n(\max)=(l/\beta_{\rm nr})(1+\beta_{\pi p}/\beta_{\rm nr})\ . \qquad (17)$$

Equations (16) and (17) lead to the following TOF distribution $F(\tau')\equiv dN/d\tau'$:[9]

$$F(\tau')=[(m_{\pi p}/2)^{1/2}\beta_{\rm nr}^2/(2l)] \times\int_{T_{\min}(\tau')}^{\infty} f(T_{\pi p})T_{\pi p}^{-1/2}dT_{\pi p}\ . \qquad (18)$$

Here $\tau'\equiv t_n-t_{\rm nr}$ is the deviation from the mean flight time. The distribution function $f(T_{\pi p})$ is assumed to be normalized so that $\int_0^\infty f(T_{\pi p})dT_{\pi p}=1$. The lower integration limit in Eq. (18) is

$$T_{\min}(\tau')\equiv m_{\pi p}\beta_{\rm nr}^4\tau'^2/(2l^2)\ . \qquad (19)$$

Equations (18) and (19) lead to a general relation[9] between the mean kinetic energy of the $\pi^- p$ atoms, $\overline{T_{\pi p}}\equiv\int_0^\infty f(T_{\pi p})T_{\pi p}dT_{\pi p}$, and the standard deviation $\sigma_{\tau'}$ of the time distribution $F(\tau')$:

$$\sigma_{\tau'}=[2\overline{T_{\pi p}}/(3m_{\pi p})]^{1/2}l/\beta_{\rm nr}^2\ . \qquad (20)$$

This equation is valid for all kinetic-energy distributions $f(T_{\pi p})$ if one neglects contributions to $\sigma_{\tau'}$ of order $l\beta_{\pi p}, l\beta_{\pi p}^3/\beta_{\rm nr}^4$, and smaller. In our case, these contributions are smaller than the dominant contribution, which is of order $l\beta_{\pi p}/\beta_{\rm nr}^2$, by several orders of magnitude.

III. EXPERIMENTAL PROCEDURE

A. Apparatus

The measurements were made at the 590-MeV proton-accelerator laboratory of the Paul Scherrer Institute. The experimental layout is shown in Figs. 1 and 2. Negative pions with a momentum of 120 MeV/c were transported by the secondary beam line $\pi E1$ to a liquid-hydrogen target assembly. There the pions passed through a CH_2 degrader, the thickness of which was optimized for maximum pion stop rate in the liquid hydrogen. This was contained in a cylindrical stainless steel cell with a length of 1.6 cm and a radius of 4.5 cm, oriented so that the cylinder axis coincided with the neutron flight direction, as indicated in Fig. 2. The flat side walls of the cell were 1 mm thick.

The incoming pions were detected by a plastic scintillator S_1, 6 cm high, 2 cm wide, and 0.3 cm thick. The plastic scintillator S_2, used as an anticounter, was 15 cm high, 15 cm wide, and 0.5 cm thick. Neutrons and photons from the liquid-hydrogen target were observed after a flight path of variable length (3–18 m) defined by a series of CH_2 and Pb collimators with round or rectangular openings.

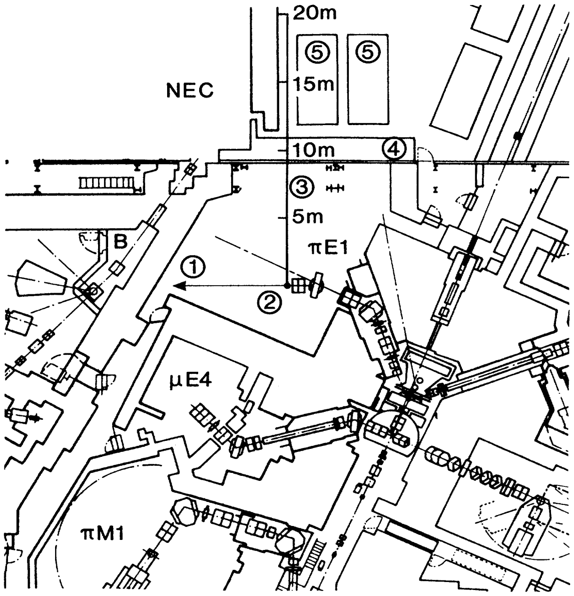

FIG. 1. Experimental area: (1) π^- beam axis; (2) liquid-hydrogen target; (3) neutron flight path; (4) shielding wall of $\pi E1$ area; (5) counting house.

The neutron detector was a NE102A organic scintillator 1.6 cm thick, 15 cm wide, and 8 cm high, viewed from opposite sides through lucite light guides by two photomultipliers. The neutron detector was shielded by CH_2 and Pb as shown in Fig. 2. The whole neutron detector assembly was mounted on a steel cart equipped with optical targets for surveying.

The neutron detector assembly contained a 2.5-cm-thick Pb converter plate, the downstream face of which

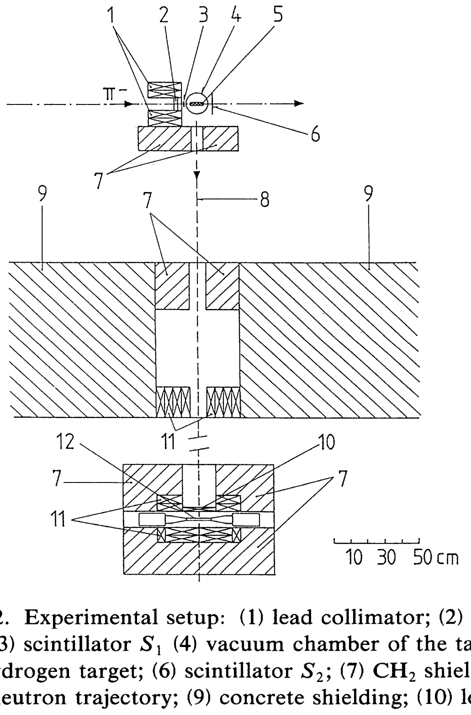

FIG. 2. Experimental setup: (1) lead collimator; (2) CH_2 degrader; (3) scintillator S_1 (4) vacuum chamber of the target; (5) liquid-hydrogen target; (6) scintillator S_2; (7) CH_2 shielding; (8) central neutron trajectory; (9) concrete shielding; (10) lead converter; (11) lead shielding; (12) scintillator S_3.

was located 5 cm upstream of the center of the scintillator. It served to convert photons from reactions (1) and (2), and also to shield the detector from charged particles. Since the mean free path of 0.42-MeV neutrons in Pb is quite large (~ 6 cm), the deterioration of the neutron TOF spectra caused by converter was tolerable.

For neutron flight paths of less than 9 meters, the neutron detector cart was mounted on the concrete floor of the $\pi E1$ area. For measurements at flight paths of more than 12 meters, the neutron flight channel led through a hole in the concrete shielding wall of the area, and the neutron detector cart was placed on a steel platform outside the experimental hall. The same signal cables from the neutron detector to the electronics shack were used in all cases. The positions of the neutron detector were measured by standard survey techniques, using theodolites and an invar wire stretched through the hole in the shielding wall. At the outside location, the distance from the wall of the experimental hall to the neutron detector was measured every few hours in order to observe shifts due to changes of ambient temperature. We measured at three distances of the neutron detector from the nominal hydrogen-target location: (1) 3.1966, (2) 7.9283, and (3) 18.1005 m. The exact position of the hydrogen target cell was neither needed nor precisely measured (cf. Sec. IV A). In contrast, the distance between positions (1) and (2) was determined to ± 0.1 mm, and that between positions (1) and (3) to ± 0.4 mm. The latter uncertainty is larger because of the temperature-dependent shifts mentioned above.

B. Electronics

1. *Pion-stop signal*

A pion stop in the target was defined by a coincidence $C_{1\pi}\cdot\overline{C}_{2\pi}$. As shown in Fig. 3, the signals $C_{1\pi}$ and $C_{2\pi}$ were defined by coincidences $S_1\cdot$rf and $S_2\cdot$rf; rf was a standard NIM signal derived from the radio frequency of the proton accelerator. The rf signals occurred at regular intervals of 19.7500 ns and could be synchronized to the 1-ns-wide pion beam bursts arriving at the target. The rf signals were delayed so that pions were accepted by the coincidence modules $C_{1\pi}$ and $C_{2\pi}$, whereas the beam contamination by electrons, which at the chosen beam momentum of 120 MeV/c arrived in bursts about halfway between the pion bursts, was suppressed. The widths and delays of the NIM pulses entering the C'_π coincidence module were chosen so that the time of the output signal of that module was determined by the RF.

The current of the 590-MeV proton beam was around 100 μA. The $C_{1\pi}$ and $C_{2\pi}$ rates defined above were 9×10^5 s^{-1} and 2.3×10^5 s^{-1}, respectively, and the electronic π^- stop rate $C_\pi \equiv C_{1\pi}\cdot\overline{C}_{2\pi}$ was 8×10^5 s^{-1}. The rate of pion stops in liquid hydrogen was only $\sim 1.4\times10^5$ s^{-1}; most of the remaining pion stops occurred in the steel walls of the liquid-hydrogen container.

2. *Neutron signal*

In the neutron detector S_3 (see Sec. III A) the signals due to the 0.4-MeV neutrons from reaction (1) produced only up to ~ 7 photoelectrons in the cathode of each of the two photomultipliers PM$_{3A}$ and PM$_{3B}$. The signals from these two photomultipliers were transmitted to constant-fraction discriminators D_{3A} and D_{3B} with thresholds corresponding to 0.6 photoelectrons from the photomultiplier cathode. A valid neutron detector signal was defined as a coincidence $C_3 \equiv D_{3A}\cdot D_{3B}$; the time of the C_3 signal was determined by D_{3B}.

At a neutron flight path of 18.1 m, the C_3 rate was 16 s^{-1}. If the proton accelerator was turned off, the C_3 rate dropped only slightly, to 14 s^{-1}. About 99.5 percent of these events were true coincidences $D_{3A}\cdot D_{3B}$, predominantly due to signal generated in the scintillator S_3 and in the Lucite light guides by cosmic muons. At a neutron flight path of 7.9 m the C_3 rate with the accelerator on

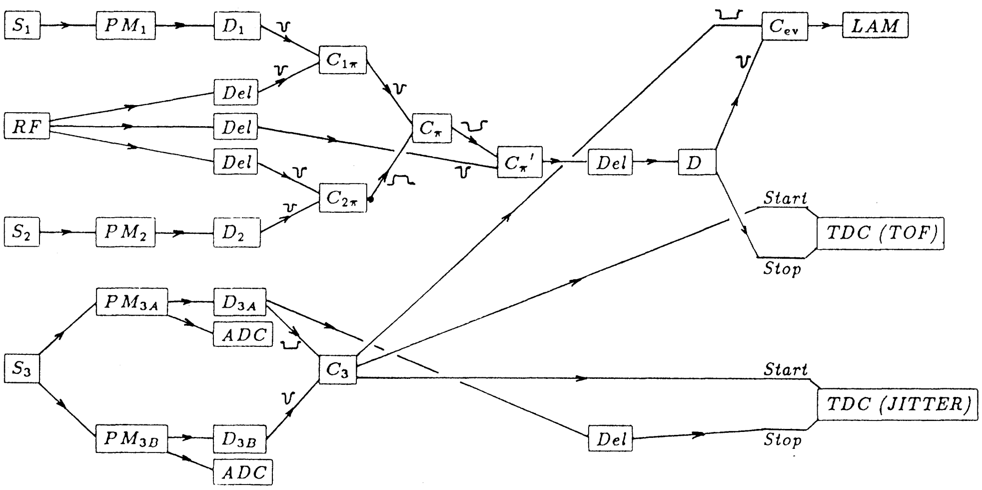

FIG. 3. Simplified block diagram of the data-taking electronics. S_i denotes scintillators; rf, the radio-frequency signal; PM$_i$, the photomultipliers; D_i, the pulse-height discriminators; Del, the delay lines; C_i, coincidence modules; ADC, the analog-to-digital converters; TDC, the time-to-digital converters; and LAM, the look-at-me signal.

was 36 s^{-1}. About 6 s^{-1} were due to photons from reaction (1) or (2) in the liquid-hydrogen target, whereas the neutrons from reactions (1) and (2) contributed only ~ 0.3 and ~ 0.13 events per second, respectively.

3. Event trigger

An event was defined by a coincidence $C_{\mathrm{ev}} \equiv C_3 \cdot C'_\pi$ (Fig. 3). The pion-stop signal C'_π (a standard NIM pulse) was first delayed in a long low-loss coaxial delay cable and then, before entering the C_{ev} coincidence module, shaped by a standard discriminator. The length of the delay cable was chosen so that the C'_π signal coincided with a C_3 signal due to a 0.4-MeV neutron generated by reaction (1) following the pion stop. Before entering the C_{ev} coincidence module, the C_3 signal was made 240 ns wide, safely wider than the 200-ns acceptance of the time-to-digital converter (TDC), so that neutron detector signals arriving up to 120 ns too early or too late also led to a C_{ev} signal. These signals were used as look-at-me (LAM) signals causing the computer to read the relevant parameters of the event. At a flight path of 18.1 m (7.9 m) the C_{ev} rate was 3 s^{-1} (7 s^{-1}). The rate of events due to reaction (1) was only 0.03 s^{-1} (0.2 s^{-1}). The remaining C_{ev} signals were due to accidental coincidences.

For each event, the output of several TDC's and analog-to-digital converters (ADC's) was written onto magnetic tape. A first TDC, labeled TDC(TOF) in Fig. 3, was started by C_3 signals and stopped by the delayed pion-stop signal C'_π. A second TDC, TDC(JITTER), was also started by C_3 signals but stopped by delayed D_{3A} signals. Since the time of the C_3 signals was determined by pulses from the discriminator D_{3B}, this second TDC recorded the time difference $(D_{3A} - D_{3B})$ for the event. The heights of the pulses from the photomultipliers PM_{3A} and PM_{3B} were recorded by ADC's.

C. Time and pulse-height distributions

1. Time distribution from TDC (TOF)

The uncorrected time distribution of the events which was recorded by the above-mentioned module TDC(TOF) at a flight path of 7.9 m is shown in Fig. 4. This distribution contains four classes of events:

(a) The peak at channel 1040 of Fig. 4 is due to neutrons from the charge-exchange reaction (1). In the events which led to this peak, the neutron signal which started the TDC and the pion-stop signal which stopped the TDC belonged to the same physical event.

(b) The narrow peaks at channels 180, 380, 580, . . . , are due to photons from the π^0 decay following reaction (1), and from reaction (2). Here, the photon that started the TDC and the π^- stopping it belonged to different events. The narrow peaks occur because of the 19.75 ns radio-frequency pion beam structure described in Sec. III B.

(c) The small peaks about halfway between the photon peaks, i.e., at channels 80, 280, 480, . . . , originate from accidental events in which the TDC was started by a neutron detector signal due to a beam electron scattered in the liquid-hydrogen target assembly; as in case (b), the TDC was stopped by a π^- in the beam.

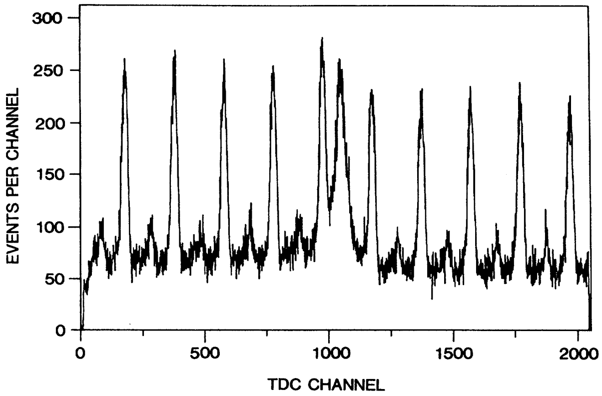

FIG. 4. Uncorrected time spectrum recorded at a flight path of $l = 7.9$ m. Abscissa: TDC channel number for photomultiplier PM_{3B}; see Fig. 3; 1 channel ≈ 0.1 ns. Ordinate: number of events per channel.

(d) The remaining events in Fig. 4 have an almost flat time distribution. Almost all of these events are accidental. The TDC was started by C_3 signals that do not exhibit an rf time structure (e.g., signals due to cosmic muons; cf. Sec. III B), and stopped by the next pion-stop signal.

The interpretation of these four classes of events was tested by moving the neutron detector away from the hydrogen target by a few centimeters; the nonaccidental neutron peak [event class (a)] moved to the left in the time distribution by the expected amount of $(0.9\ \mathrm{cm/ns})^{-1}$, whereas the photon peaks [class (b)] moved only by $(30\ \mathrm{cm/ns})^{-1}$. If the hydrogen target cell was emptied, the nonaccidental neutron peak and the photon peaks [event classes (a) and (b)] disappeared, whereas the remainder of the spectrum [classes (c) and (d)] changed only slightly.

2. Two-dimensional distribution from TDC (TOF) and ADC (PM_{3B})

The two-dimensional distribution shown in Fig. 5 contains the same events as Fig. 4. It is based on the TDC(TOF) output and the ADC output of the photomultiplier PM_{3B}; see Fig. 3. The four classes of events defined above are also visible in Fig. 5:

(a) The events due to reaction (1) appear at TDC channel 1040 and reach up to ADC channel ~ 800, corresponding to ~ 7 photoelectrons. For further analysis, the pulse-height region of charge-exchange neutron events in Fig. 5, and also at the other flight distances, was defined to lie between ADC channels 170 and 950. These cuts removed most of the background due to single photoelectron signals and the background due to large signals.

(b) The accidental photon events at channels 770, 970, . . . have a broad pulse-height distribution extending above the top of Fig. 5. A further ADC, not shown in Fig. 3, was fed with attenuated signals from PM_{3B}. The resulting photon pulse-height distribution has a minimum

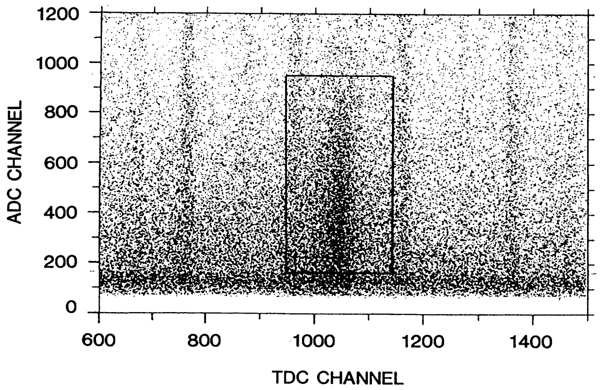

FIG. 5. Two-dimensional event distribution recorded at $l=7.9$ m. Horizontal coordinate: TDC channel number for photomultiplier PM_{3B}; vertical: ADC channel number for photomultiplier PM_{3B}. The rectangle drawn near the center of the figure contains the events which were used to derive the TDC(JITTER) distribution, described in Sec. III C 3.

at ~70 photoelectrons and a subsequent broad maximum at ~90 photoelectrons. The position of this maximum was used to verify that no significant photomultiplier gain drifts occurred during data taking. Such gain drifts could have led to time shifts because the electronic transit time from scintillator S_3 to the output of the constant-fraction discriminator D_{3A} or D_{3B} depends slightly on pulse height. This dependence can be determined from the inclination of the bands due to the neutron and photon events in Fig. 5.

(c) The beam electron events are visible in Fig. 5 as faint bands at TDC channel 670,870, . . . ; like class (b) events, they have a pulse-height distribution extending above the top of the figure.

(d) The events without rf time structure are dominated by a horizontal band at ADC channel 120 in Fig. 5. This band is due to single electrons from the photocathode of PM_{3B}.

3. *Distribution of the time difference* $[t(PM_{3A})-t(PM_{3B})]$

The TDC(JITTER) distribution of the charge-exchange neutron events is shown as a histogram in Fig. 6. These events satisfied the pulse-height criteria specified above. In addition, they were required to lie in a 20-ns-wide time region of the TDC(TOF) distribution including the charge-exchange neutron peak. The selected events are thus inside the rectangle in the two-dimensional distribution shown in Fig. 5. The remaining accidental background was determined by averaging the TDC(JITTER) distributions of the events in two other retangles of the same dimensions, shifted in time from the rectangle shown in Fig. 5 by $\pm 3\times 19.75$ ns. The distribution obtained after this background subtraction (Fig. 6) was used in the data analysis to determine the distribution of the time from the light signal in the scintillator S_3 of the neutron detector to the start of TDC(TOF); see Sec. IV F.

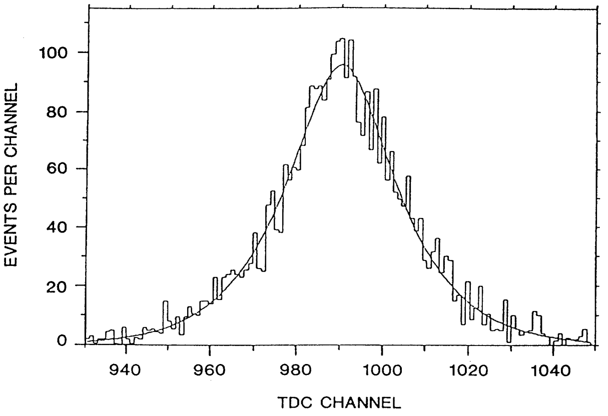

FIG. 6. Histogram: experimental TDC(JITTER) distribution, related to time differences between signals from photomultipliers PM_{3A} and PM_{3B}, after background subtraction (Sec. III C 3). Curve: fitted function $g(t_J)$ of Sec. IV F.

IV. DATA ANALYSIS

A. Principle of the analysis

Our method of determining the neutron velocity v_{nr} (see Sec. II A) is similar to that of Ref. 10. However, the older method depended on the measurement of signal velocities in the coaxial delay cables, whereas in our case this time standard is replaced by the precisely known radio-frequency structure of the pion beam. The charge-exchange neutron velocity v_{nr} is derived from the position of the neutron peak in the TOF spectra (Fig. 4) relative to the pattern of the accidental photon peaks. These peaks are known to occur at regular intervals of $\tau_{\mathrm{rf}}=19.750\,034\pm0.000\,002$ ns. This period and its uncertainty were determined by observation of two independent high-precision frequency meters connected to the radio-frequency master oscillator of the proton accelerator.

In each TOF spectrum (e.g. Fig. 4) a time axis τ was defined, the origin of which was chosen to coincide with a photon peak about 30 ns before the charge-exchange neutron peak. In Fig. 4 this origin is at TDC channel ~1370; the τ axis in this figure points to the left. The charge-exchange neutron peak is predicted to occur at

$$\tau=\tau_{\mathrm{nr}}\approx l/v_{\mathrm{nr}}-l/c-I'\tau_{\mathrm{rf}}\ . \tag{21}$$

Here l is the flight path from the hydrogen target cell to the neutron detector; l/v_{nr} is the flight time of a neutron produced by reaction (1) in a hydrogen atom at rest; l/c is the flight time of photons, and I' is an integer equal to the number of radio-frequency periods τ_{rf} between the accidental photon peak at $\tau=0$ and the nonaccidental photon peak. This latter peak is outside the TDC range of Fig. 4, but its position, i.e., the integer I', can be calculated from an approximate knowledge of the signal transit times in the delay cables and the electronics modules. Equation (21) is not rigorous because of effects due to the difference between the signals generated in the scintillator S_3 by neutrons and photons. These effects cancel if v_{nr} is determined from the difference $\tau_{\mathrm{nr},2}-\tau_{\mathrm{nr},1}$ of the neutron peak positions measured at two different flight paths l_1 and l_2. In this case, Eq. (21) leads to the exact equation

$$v_{\mathrm{nr}}=\{[\tau_{\mathrm{nr},2}-\tau_{\mathrm{nr},1}+(I_2'-I_1')\tau_{\mathrm{rf}}]/(l_2-l_1)+1/c\}^{-1} . \tag{22}$$

B. Distribution of mean time from the two photomultipliers of the neutron detector

In order to improve the precision of the time-of-flight measurements, the time distributions discussed in Sec. III C were used to derive, for each event, the time t_m between the pion-stop signal and the mean time of the signals from the two photomultipliers of the neutron detector. The resulting distribution of the mean-time channel number N_m for the events in Fig. 4, recorded at a flight distance of 7.9 m, is shown in Fig. 7(a). The peaks are narrower in Fig. 7(a) than in Fig. 4 for two reasons: first, the time spread due to the difference in light paths arising from the finite size of the scintillator S_3 is reduced by the time-averaging process outlined above; second, in Fig. 7(a) a larger number of photoelectrons, from the cathodes of both photomultipliers PM_{3A} and PM_{3B}, contribute to the time measurement.

In Figs. 7(b) and 7(c) the mean-time spectra of Fig. 7(a) for events in two different pulse-height regions are shown. Figure 7(b) contains events in which the PM_{3B} pulse height was in the charge-exchange neutron region, i.e., between ADC channels 170 and 950; see Figs. 3 and 5. Figure 7(c) contains events where this pulse height is ≥ 1200 ADC channels.

C. The photon peaks

The time distribution in Fig. 7(c) is seen to be dominated by the photon peaks (TDC channels 180,380, . . .) and the smaller electron peaks (TDC channels 80,280,480,. . . .; see Sec. III C 1). The photon peaks were used to determine the origin of the time axis τ, defined in Sec. IV A. For background subtraction, a straight line was fitted to the regions of the spectrum in Fig. 7(c) between the photon and electron peaks. The time spectrum for large pulse heights after the subtraction of this background is shown in Fig. 8. For clarity only a part of the spectrum is displayed in Fig. 8. The whole spectrum contains 10 photon peaks, labeled $\gamma_1,\gamma_2,\ldots,\gamma_{10}$. For each of these 10 photon peaks a 50-channel wide peak region was selected, and the mean and the variance of the corresponding 50-channel histogram was calculated. The 10 mean channel numbers $\overline{N_i}$ (where $i=1,2,\ldots,10$) were fitted by straight line

$$\overline{N_i}=a+bi . \tag{23}$$

This fit gave $\chi^2=10.4$ for 8 degrees of freedom. The resulting parameters are

$$a=-20.47\pm0.12,\quad b=198.760\pm0.018 . \tag{24}$$

These parameters a and b and their uncertainties were used to calculate the TDC channel number $N_{(\tau=0)}$ corresponding to the origin $\tau=0$, and its uncertainty.

The parameter b given in Eq. (24) was also used to determine the TDC calibration: 198.760±0.018 TDC channels correspond to the radio-frequency period $\tau_{\mathrm{rf}}=19.750\,034\pm0.000\,002$ ns. One average TDC channel thus corresponds to

$$\overline{\tau}_{\mathrm{ch}}=\tau_{\mathrm{rf}}/b=0.099\,366\,2\pm0.000\,009\,0\ \mathrm{ns} . \tag{25}$$

This result agrees with the value 0.100±0.001 ns given by

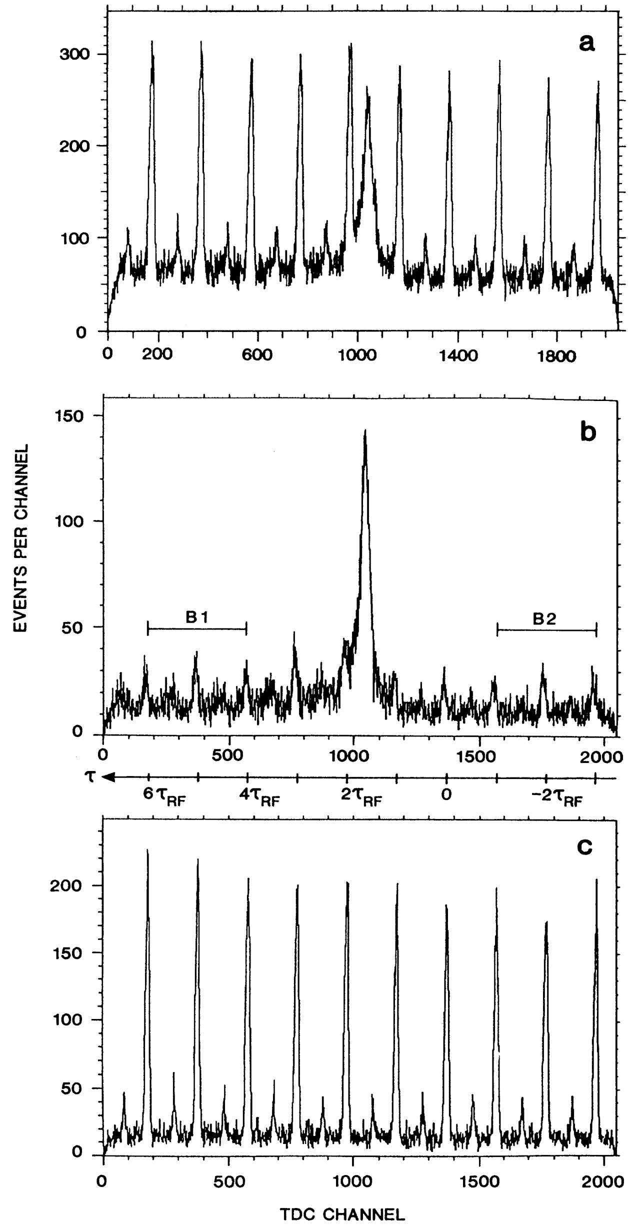

FIG. 7. Mean-time spectra recorded at $l=7.9$ m for all pulse heights (a), for small pulse heights (b), and for large pulse heights (c). Abscissa: mean TDC channel number; Ordinate: number of events per channel. The τ axis drawn between histograms (b) and (c) is discussed in Sec. IV A. The two regions B1 and B2 indicated in histogram (b) were used to calculate the accidental background (Sec. IV D).

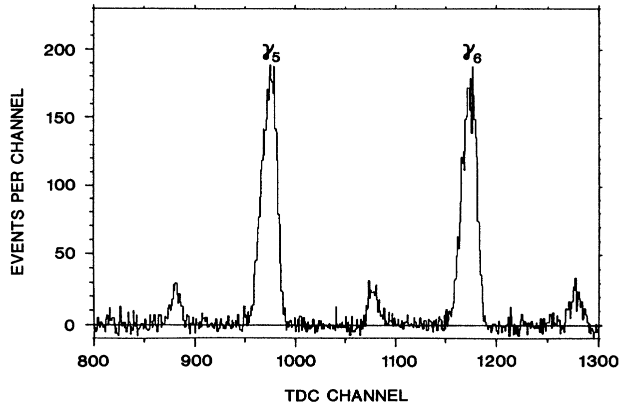

FIG. 8. As Fig. 7(c), after background subtraction; see Sec. IV C.

the manufacturer, Lecroy Inc., of the TDC type 2228A.

The standard deviations $\sigma_{\gamma i}$ (i.e., the square roots of the variances) of the ten 50-channel histograms are consistent with each other ($\chi^2=9.3$ for 9 degrees of freedom) and have a mean

$$\bar{\sigma}_\gamma=0.692\pm0.006 \text{ ns} . \tag{26}$$

The largest contribution to this photon peak width is the spread of the time between a $\pi^- p\rightarrow\pi^0 n$ reaction in the hydrogen target and the corresponding radio-frequency signal which determines the time of the pion-stop signal (see Sec. III B). A second contribution to $\bar{\sigma}_\gamma$ is the spread of the signal transfer time from the scintillator S_3 to the TDC's.

At a flight path of 3.2 m (18.1 m) we found $\bar{\sigma}_\gamma=0.690\pm0.015$ ns (0.720 ± 0.011 ns). The standard deviation at 18.1 m is slightly larger than at the two smaller distances because of small time drifts of the pion beam signal from scintillator S_1 relative to the rf, observed during the data taking at 18.1 m. The corresponding additional time spread was taken into account as described in Sec. IV H.

D. The neutron peak

The time distribution shown in Fig. 7(b) is dominated by the peak due to neutrons from the reaction $\pi^- p\rightarrow\pi^0 n$. In order to calculate the accidental background under this peak, we used the fact that according to our Monte Carlo simulation (see Sec. IV E) the tails of the neutron peak are insignificant at times more than 50 ns before or after the peak. The accidental background was determined by fitting a function $u(N)$ of the TDC channel number N to the two regions B1 and B2, indicated in Fig. 7(b), where $180\leq N\leq 577$ and $1573\leq N\leq 1970$, respectively. The function $u(N)$ was defined as

$$u(N)\equiv u_0(K)e^{-AI} . \tag{27}$$

Here, the integer K ranges from 0 to 199 and is equal to the number of a TDC channel counted from the start of a period of 199 channels ($\approx\tau_{\mathrm{rf}}$), and the integer I is the number of the period. The two regions B1 and B2 of the spectrum used for the determination of the background (see above) correspond to the four periods $I=1$, 2, 8, and 9. The parameter A occurring in Eq. (27) is a small constant related to the average rate of the pion-stop signals. The choice of this form of $u(N)$ takes into account that a part of the accidental background in Fig. 7(b), e.g., the accidental photon and electron peaks, is due to accelerator-related events.

In Eq. (27) the period τ_{rf} is assumed to correspond to exactly 199 TDC channels, whereas the period calculated as described in Sec. IV C is 198.76 channels. This inaccuracy could have been avoided by rebinning the data. However, since the neutron peak region in Fig. 7(b) is about halfway between the two regions used for the determination of the background, the time shifts caused

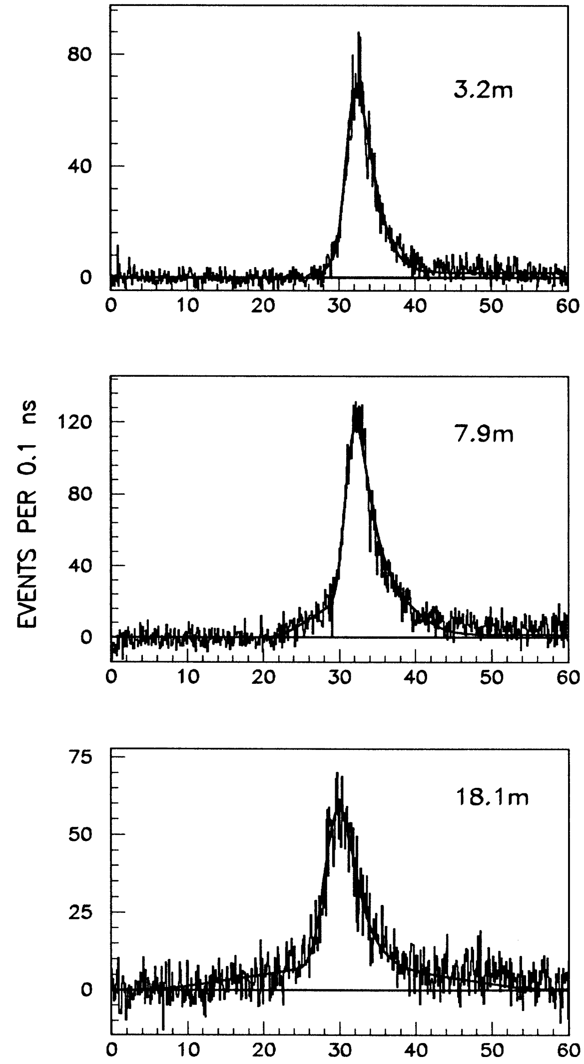

FIG. 9. Histograms: experimental time-of-flight spectra of neutrons from charge exchange $\pi^- p\rightarrow\pi^0 n$, after background subtraction, for flight paths of 3.2, 7.9, and 18.1 m. Time, in ns, is from an accidental photon peak about 30 ns before the neutron peak. Curves: theoretical distributions fitted to the data.

by our simplification are negligible.

The resulting τ distribution at a flight path of 7.9283 m is shown in Fig. 9, together with the analogous spectra for flight paths of 3.1966 m and 18.1005 m. In view of Fig. 9 the background subtraction procedure just outlined appears adequate: The spectra are consistent with zero in the regions more than ~20 ns before the neutron peaks, and the accidental photon and electron peaks visible in Fig. 7(b) have disappeared as expected.

The tails to the right of the neutron peaks in Fig. 9 are due not only to the finite kinetic energies of the $\pi^- p$ atoms before the reaction $\pi^- p \rightarrow \pi^0 n$, but also to neutrons which have reached the neutron detector after scattering in the materials in and around the flight channel. In contrast, the tail to the left of the neutron peak is not contaminated by neutron scattering; this tail, not visible at 3.2 m, extends to about 10 ns (20 ns) before the peak at 7.9 m (18.1 m). As discussed in Sec. II B, these tails correspond to a kinetic-energy distribution $f(T_{\pi p})$ of the $\pi^- p$ atoms which extends up to ~70 eV.

E. Monte Carlo simulation

In order to determine the velocity v_{nr} of neutrons, produced in the reaction $\pi^- p \rightarrow \pi^0 n$, Monte Carlo–generated TOF spectra were fitted to the corresponding experimental ones, for the three neutron flight distances of the experiment. The spatial distribution, resulting from our Monte Carlo program,[11,12] of π^- stops within the 1.6-cm-wide liquid-hydrogen target is homogeneous in the direction of the neutron flight channel (Fig. 2). In the π^- beam direction the stop density decreases with distance, and in the vertical direction the distribution is symmetrical and peaked at the center, as expected. The initial velocity of the charge-exchange neutrons is assumed to have a fixed magnitude of 0.8942 cm/ns and an isotropic angular distribution. The program treats neutron energy loss through scattering in the LH_2 target, the collimator jaws, the air on the flight path, the lead converter, the neutron detector, and the shielding of the neutron detector.

The resulting times from the production of a neutron in the LH_2 target to a detectable np scattering in the scintillator S_3 were stored in histograms, for each of the three flight distances. In a 5-ns-wide region of time, centered on the charge-exchange neutron peak, about 70% of these Monte Carlo–generated events are due to neutrons which are not scattered between the hydrogen target and S_3. Most of the remaining 30% of the neutrons in the peak region were scattered only in the neutron detector assembly. Therefore the shape of the Monte Carlo–generated time distribution in the peak region is almost the same for each of the three flight distances.

F. Electronic time jitter

The histograms generated by the Monte Carlo program were folded with the time distribution due to the jitter of the electronic transit time from the np scattering in the scintillator S_3 to the TDC input signals. Tests with a light pulser showed that the distribution function $f_{\mathrm{el}}(t)$, where t is the time from the light pulse to the TDC(TOF) input signal, depends strongly on the intensity of the light pulse. The shape of the time distribution of the charge-exchange neutron events was derived from the data by use of the model

$$f_{\mathrm{el}}(t) = f_0'(1-e^{-a't})^2 e^{-b't} , \tag{28}$$

found to fit the data, where $f_0' = b'(a'+b')(2a'+b')/2a'^2$, so that $\int_0^\infty f_{\mathrm{el}}(t)dt = 1$. The shape of the distribution $f_{\mathrm{el}}(t)$ can be assumed to be approximately valid also for each of the two times t(start) and t(stop) from the np scattering in S_3 to one of the two inputs of the TDC(JITTER) (see Fig. 3). An equation for the distribution $g(t_J)$ of time differences $t_J \equiv t(\mathrm{stop}) - t(\mathrm{start})$ was derived from Eq. (28), under the simplifying assumption that the distributions of t(start) and t(stop) around their means are uncorrelated. Then the parameters a' and b' were determined by fitting the function $g(t_J)$ to the measured distribution shown in Fig. 6. The values of the constants a' and b' found for the three flight distances of the experiment are consistent with each other, as expected. In the analysis of the spectra in Fig. 9 (cf. Sec. IV H), we used the mean values

$$a' = 1.268 \pm 0.014 \ \mathrm{ns}^{-1}, \quad b' = 0.847 \pm 0.017 \ \mathrm{ns}^{-1} \tag{29}$$

for each of the three distances. Finally the distribution $h(t_m)$, where $t_m \equiv (t_{3A} + t_{3B})/2$ is the mean time defined in Sec. IV B, was derived from Eq. (28) and folded with the Monte Carlo–generated histogram mentioned above. The distortions caused by the assumption of uncorrelated time distributions mentioned above were treated by introducing a distance-independent Gaussian time distribution of adjustable width, as described in Sec. IV H.

G. Broadening of time distribution with distance

As the next step, the theoretical time distributions were folded with the distance-dependent distribution $F(\tau')$ due to the kinetic energy of the $\pi^- p$ atoms, discussed in Sec. II B. A kinetic-energy distribution $f(T_{\pi p})$ found to agree with the data is shown in Fig. 10, together

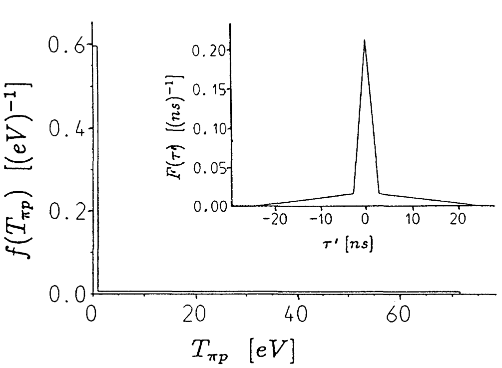

FIG. 10. Distribution function $f(T_{\pi p})$ found to fit the neutron TOF spectra of Fig. 9; $T_{\pi p}$ is the kinetic energy of the $\pi^- p$ atoms just before the charge-exchange reaction (1); $F(\tau')$ is the corresponding neutron TOF distribution for a flight path of 18.1 m.

with the corresponding function $F(\tau)$ for a flight path of 18.1 m, calculated from Eq. (18). The model used for the function $f(T_{\pi p})$ was

$$f(T_{\pi p})=\eta/T_i, \quad \text{if } 0<T_{\pi p}<T_1 \ ,$$
$$f(T_{\pi p})=(1-\eta)/(T_2-T_1), \quad \text{if } T_1<T_{\pi p}<T_2 \ , \qquad (30)$$
$$f(T_{\pi p})=0, \quad \text{if } T_2<T_{\pi p} \ .$$

The three free parameters of this model are η, T_1, and T_2.

H. Fit to the data

The curves in Fig. 9 were obtained by fitting nine free parameters simultaneously to all three experimental spectra. The free parameters were as follows.

(1) The neutron velocity v_{nr} for $\pi^- p$ atoms at rest. The deviation of v_{nr} from the value assumed in the Monte Carlo program (Sec. IV E) leads to shifts of the theoretical time distributions.

(2) The distance from the hydrogen target to the neutron detector at the position labeled "3.2 m" in Fig. 9, which in contrast with the distances between the three positions was neither needed nor precisely measured. This free parameter also served to take into account the distance-independent electronic transit time difference (scintillator S_3 to TDC) for neutron and photon signals.

(3) The standard deviation σ_t of a Gaussian time distribution, which was folded with the theoretical distributions described in Sec. IV E–IV G. The optimal value of this standard deviation found by the fit is smaller than that due to the spread of the differences between the time of reaction (1) and that of the corresponding π^- beam telescope signal. This can be attributed to the simplifying assumption of uncorrelated PM_{3A} and PM_{3B} time distributions discussed in Sec. IV F.

(4,5,6) Three normalization factors for the ordinates (events per TOF bin) of the three spectra shown in Fig. 9.

(7,8,9) The three free parameters of the kinetic-energy distribution function $f(T_{\pi p})$; see Eq. (30).

The electronic time-jitter constants a' and b' discussed in Sec. IV F were treated as fixed parameters. Their uncertainties $\Delta a'$ and $\Delta b'$ [cf. Eq. (29)] were neglected, since they were included with sufficient accuracy by the error of the the free parameter (3) defined above. At 18.1 m, the square σ_t^2 of this parameter was made larger than at the two smaller distances by a fixed amount, which was calculated from the measured mean standard deviations $\overline{\sigma_\gamma}$ of the photon peaks; cf. Sec. IV C.

The theoretical time distributions of the best fit are shown by smooth curves in Fig. 9. The fit was restricted to the time bins of Fig. 9 from 0 to 40 ns in order to be insensitive to imperfections in the Monte Carlo predictions of the tails due to neutron scattering. The minimum of χ^2 was found by the program MINUIT.[13] The statistical uncertainties of the optimized free parameters were determined by taking the average of the positive and negative errors calculated by the subroutine MINOS of MINUIT. The χ^2 value of the best fit was 1265 for 1191 degrees of freedom. These numbers were used to determine a "scale factor" $S=(1265/1191)^{1/2}=1.031$, by which the parameter errors resulting from MINOS were multiplied. The fact that χ^2 per degree of freedom is slightly larger than 1 can be attributed to the approximate method of calculating the background function $u(N)$, described in Sec. IV D.

V. RESULTS

The resulting velocity of neutrons from the charge exchange in $\pi^- p$ atoms at rest is

$$v_{\text{nr}}=0.894\,266\pm 0.000\,063 \text{ cm/ns} \ . \qquad (31)$$

The uncertainty Δv_{nr} of Eq. (31) was obtained by quadratic addition of five contributions: the first, due to experimental statistics (see Sec. IV H) is $\pm 4.4\times 10^{-5}$ cm/ns, corresponding to about 2% of the line widths in Fig. 9; the second, due to the neutron-detector distance measurements, is $\pm 2.4\times 10^{-5}$ cm/ns; the third, due to the statistical uncertainties of the Monte Carlo–generated theoretical time distributions, is $\pm 3.0\times 10^{-5}$ cm/ns; the fourth, due to the uncertainties of the accidental photon-peak positions used to define the origins ($\tau=0$) in Fig. 9, is $\pm 1.0\times 10^{-5}$ cm/ns; the fifth contribution to Δv_{nr} is related to possible photomultiplier gain drifts; as discussed in Sec. III C 2, these drifts were found to be consistent with zero; the corresponding contribution to Δv_{nr} is $\pm 2.1\times 10^{-5}$ cm/ns.

The pion mass difference calculated from Eqs. (5) and (31) is

$$D_\pi=m_{\pi^-}-m_{\pi^0}=4.593\,64\pm 0.000\,48 \text{ MeV} \ . \qquad (32)$$

The uncertainty in Eq. (32) is the quadratic sum of the uncertainty due to Δv_{nr}, $\pm 4.7\times 10^{-4}$ MeV [calculated from Eqs. (6) and (31)], and that due to the uncertainty of the mean binding energy $\overline{E_B}$, $\pm 0.8\times 10^{-4}$ MeV [calculated from Eqs. (11) and (12)].

Subtraction of the mass difference of Eq. (32) from the π^- mass value,[4] $139.567\,37\pm 0.000\,33$ MeV, gives the π^0 mass value

$$m_{\pi^0}=134.973\,73\pm 0.000\,58 \text{ MeV} \ . \qquad (33)$$

It should be noted that the π^- mass value just quoted, which is derived from pionic-atom x-ray energies, is smaller by 1.8 standard deviations than the π^+ mass value 139.5694 ± 0.0011 MeV calculated from the muon mass[4] and the muon momentum p_{μ^+} in pion decay at rest[14] under the assumption of a vanishing muon-neutrino mass. For nonzero neutrino mass, the resulting π^+ mass would be even larger. If one assumes $m_{\pi^-}=m_{\pi^+}$ according to the CPT theorem, the quoted π^+ mass value and Eq. (31) lead to the neutral-pion mass

$$m_{\pi^0}=134.9759\pm 0.0012 \text{ MeV} \ . \qquad (34)$$

Preliminary results of a new p_{μ^+} measurement[15] confirm the π^+ mass quoted above and increase the significance of its deviation from the m_{π^-} value[4] to >3 standard deviations.

The resulting parameters for the kinetic-energy distribution $f(T_{\pi p})$ of the $\pi^- p$ atoms according to Eq. (30) are

$$\eta = 0.559 \pm 0.013, \quad T_1 = 0.94 \pm 0.13 \text{ eV}, \quad T_2 = 71.5 \pm 6.1 \text{ eV}. \tag{35}$$

The corresponding mean kinetic energy of the $\pi^- p$ atoms is

$$\overline{T_{\pi p}} = T_1/2 + (1-\eta)T_2/2 = 16.2 \pm 1.3 \text{ eV}. \tag{36}$$

The distribution function $f(T_{\pi p})$ presented in Fig. 10 and in Eqs. (30) and (35) consists of two components, the first of which reaches from zero to $T_1 = 0.94 \pm 0.13$ eV and contains $\eta = 55.9 \pm 1.3$ percent of the $\pi^- p$ atoms; the second component, containing the remainder of the $\pi^- p$ atoms, reaches from T_1 to $T_2 = 71.5 \pm 6.1$ eV. In this model both components of the kinetic energy distribution are assumed to be flat. Since the experimental spectra are of limited statistical accuracy, they do not exclude $T_{\pi p}$ distributions which differ somewhat from that defined by Eqs. (30) and (35); however, the extension of the time-of-flight tails in Fig. 9 implies model independently that the $T_{\pi p}$ distribution extends up to ~70 eV.

The high-energy component of the distribution $f(T_{\pi p})$ may be due to Coulomb deexcitation[3] of the $\pi^- p$ atom near one of the protons of the surrounding liquid hydrogen. In this process the deexcitation energy is partly transformed into kinetic energy of the $\pi^- p$ atom; the energy $T_{\pi p}$ of $\pi^- p$ atoms which have just undergone the $5 \rightarrow 4$ $(4 \rightarrow 3)$ Coulomb deexcitation is around 30 eV (70 eV).

VI. COMPARISON WITH PREVIOUS RESULTS

A. Pion mass difference

The new result for the mass difference D_π given by Eq. (32) is lower than the 1986 world average (Ref. 1), 4.6043 ± 0.0037 MeV, by 2.9 standard deviations. The 1986 world average was based mainly on Refs. 10 and 16.

In contrast, Eq. (32) agrees well with our previous result (Ref. 17), 4.5930 ± 0.0013 MeV, which was obtained from neutron TOF distributions recorded at flight distances of 2.819 and 8.440 m. For Ref. 17, the pion beam momentum, the shape and size of the neutron detector scintillator, and also the type of photomultiplier used, differed from those of the present experiment.

B. Kinetic energy distribution of $\pi^- p$ atoms

The neutron velocity spread derived by Czirr[10] corresponds to the mean kinetic energy $\overline{T_{\pi p}} = 115 \pm 43$ eV. This is incompatible with the new result given in Eq. (36), 16.2 ± 1.3 eV.

The new $\overline{T_{\pi p}}$ value of Eq. (36) is higher by 2.1 standard deviations than our previous result (Ref. 17), 6.2 ± 4.6 eV, which was obtained on the assumption of Gaussian time distributions. The analysis of Ref. 17 was restricted to the peak region of the charge-exchange neutron TOF distributions. A recent reanalysis[18] of the data of Ref. 17, including larger time windows around the neutron peaks, yielded the time distributions shown in Fig. 11. The mass difference D_π found in that reanalysis agrees with Ref. 17. However, the 8.4 m histogram of Fig. 11 contains a significant tail, extending to ~10 ns before the peak, which was overlooked in the original analysis.[17] The kinetic-energy distribution $f(T_{\pi p})$ corresponding to Fig. 11 is similar to that defined by Eqs. (30) and (35), confirming a high-energy component of $f(T_{\pi p})$ which contains about half of the $\pi^- p$ atoms.[18]

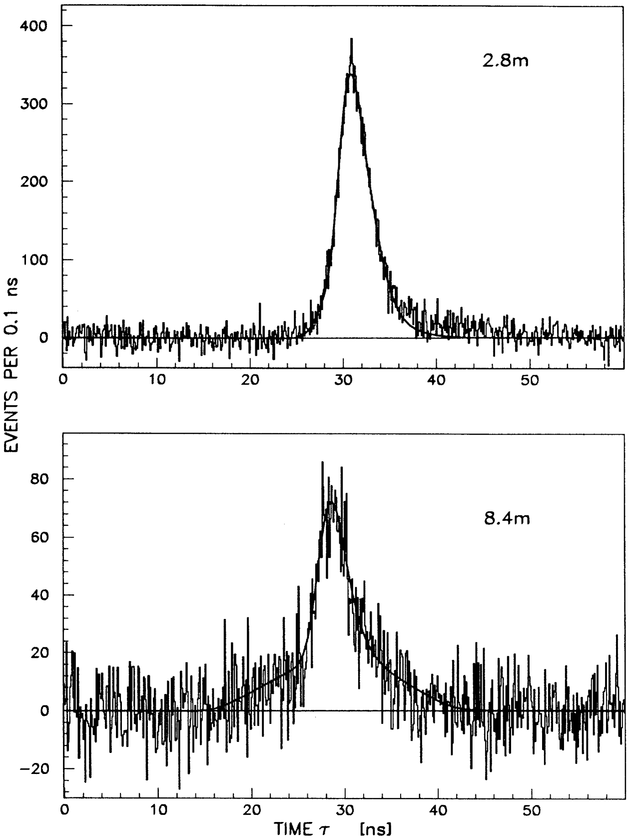

FIG. 11. As Fig. 9, but for data of Ref. 17, obtained at flight paths of 2.819 and 8.440 m.

VII. TIME-OF-FLIGHT OF NEUTRONS FROM RADIATIVE PION CAPTURE

The measured time-of-flight of neutrons from radiative capture, $\pi^- p \rightarrow \gamma n'$, can be used to determine the mass m_{π^-} of the π^- meson. While the result is less accurate than the m_{π^-} values derived from measured energies of x-rays emitted by pionic atoms, the comparison of the two m_{π^-} values tests our method of measuring neutron velocities.

Our measurement of the velocity $v_{n'r}$ of the radiative-capture neutrons, for $\pi^- p$ atoms at rest, was similar to the v_{nr} measurement described in Secs. III and IV. The data for the two reactions (1) and (2) were taken simultaneously by use of two separate electronic circuits of the type shown in Fig. 3. For radiative capture, the coaxial delay line at the output of the coincidence module C'_π

was shorter than for charge exchange.

The uncorrected n' time distributions recorded at the three flight distances are shown in Fig. 12. The top histogram contains a high peak around channel 1300, which is due to nonaccidental photons from reactions (1) and (2), i.e., to cases in which the TDC start and stop signals are caused by the same event. In addition, the top histogram exhibits a broad peak, in channels 800–1200, attributed predominantly to nonaccidental neutrons n'' emitted after π^- capture by the iron nuclei of the liquid-hydrogen target vessel. The tail of this broad peak is also visible in the histogram recorded at 7.9 m. The radiative-capture neutrons n' lead to nonaccidental peaks in channel ~ 650 in each of the three histograms.

The background subtraction, similar to that for the charge-exchange neutrons, resulted in the n' time distributions shown in Fig. 13. Here the origins of the time axes are at the accidental photon peaks immediately preceding the good n' peaks. The peak regions of the experimental spectra, which were used to determine the velocity $v_{n'r}$, are indicated by cross-hatched histograms. The smooth curves in Fig. 13 represent the theoretical time distributions fitted to the data. In the case of the radiative-capture neutrons, the Monte Carlo time distributions described in Sec. IV E were replaced by "theoretical" distributions, the shape of which was obtained by folding a Gaussian distribution with the $(t>0)$ part of an exponential distribution $e^{-t/T'}$. The standard deviation σ' of the Gaussian distribution and the time constant T' of the exponential distribution were assumed to be distance independent, and were treated as free parameters in the fit to the experimental data. This fit was done twice, first without and then with inclusion of the broadening of the theoretical TOF peaks with distance, due to the kinetic-energy distribution $f(T_{\pi p})$ defined by Eqs. (30)

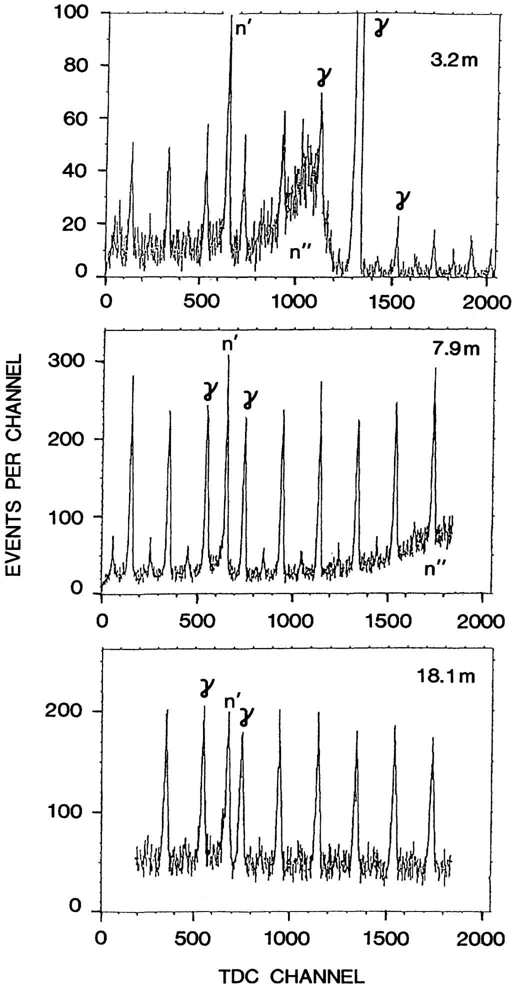

FIG. 12. Uncorrected time spectra containing, in channel ~ 650, the nonaccidental peak due to neutrons from radiative capture, $\pi^- p \rightarrow \gamma n'$. Other structures of these spectra are discussed in Sec. VII.

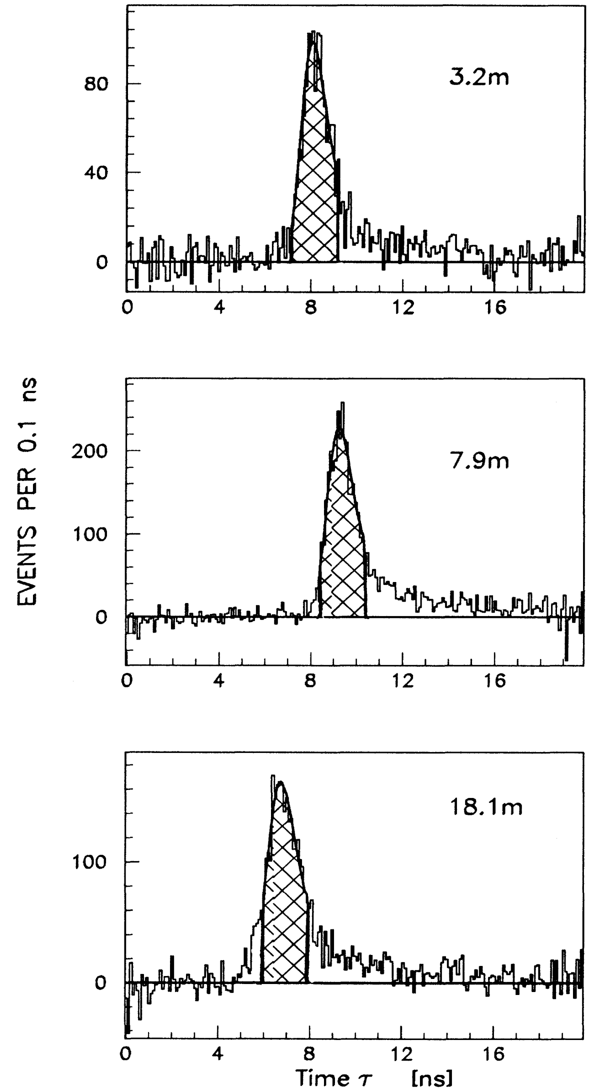

FIG. 13. Time distributions of radiative-capture neutrons derived from Fig. 12. The origins of the time axes are at the preceding accidental photon peaks. Histograms: experimental data. Curves: fitted theoretical distributions.

and (35). From Eqs. (18)–(20) it follows that at a given flight path the width of the time distribution $F(\tau')$ for radiative-capture neutrons is narrower than that for charge-exchange neutrons by a factor $(v_{\mathrm{nr}}/v_{\mathrm{n'r}})^2 = 0.0478$. The χ^2 value of the fit illustrated in Fig. 13 improved from 69.7 to 64.5 for 56 degrees of freedom by the inclusion of the broadening.

The neutron velocity found by the fit with broadening is

$$v_{\mathrm{n'r}} = 4.090\,96 \pm 0.000\,76 \text{ cm/ns} . \quad (37)$$

The uncertainty $\Delta v_{\mathrm{n'r}}$ of Eq. (37) was obtained by quadratic addition of four contributions, due to (1) experimental statistics (±0.000 43 cm/ns), (2) neutron-detector distance measurements (±0.000 11 cm/ns), (3) determination of origins of time axes in Fig. 13 (±0.000 38 cm/ns), and (4) possible photomultiplier gain drifts (±0.000 49 cm/ns). The π^- mass value derived from Eq. (37),

$$m_{\pi^-} = 139.589 \pm 0.028 \text{ MeV}/c^2 , \quad (38)$$

agrees well with the world average;[4] since the uncertainty is dominated by the velocity uncertainty of Eq. (37), the agreement can be regarded as evidence for the adequacy of our method to measure $v_{\mathrm{n'r}}$ to a relative uncertainty

$$\Delta v_{\mathrm{n'r}}/v_{\mathrm{n'r}} = \pm 2 \times 10^{-4} . \quad (39)$$

In comparison, the deviation of our result for the pion mass difference [Eq. (32)] from the 1986 world average corresponds to a relative deviation of the charge-exchange neutron velocity of $\Delta v_{\mathrm{nr}}/v_{\mathrm{nr}} = (16 \pm 6) \times 10^{-4}$.

ACKNOWLEDGMENTS

This experiment benefited from discussions with Dr. P. F. A. Goudsmit and Dr. L. M. Simons, and from the excellent assistance by many Paul Scherrer Institute staff members. We thank R. Balsiger, P. Gheno, P. Gross, P. Hug, and Dr. D. Renker for their work on the liquid-hydrogen target, and P. Hayes for his cooperation in the data taking. The experiment was supported in part by a grant from the U.S. Department of Energy.

---

*Present address: CERN, CH-1211 Genève 23, Switzerland.

[1] Particle Data Group, M. Aguilar-Benitez *et al.*, Phys. Lett. **170B**, 1 (1986).

[2] J. F. Crawford *et al.*, Phys. Lett. B **213**, 391 (1988).

[3] L. I. Men'shikov, Muon Catalyzed Fusion **2**, 173 (1988).

[4] Particle Data Group, J. J. Hernández *et al.*, Phys. Lett. B **239**, (1990).

[5] M. Leon and H. A. Bethe, Phys. Rev. **127**, 636 (1962).

[6] B. Budick *et al.*, Phys. Lett. **34B**, 539 (1971).

[7] E. Borie and M. Leon, Phys. Rev. A **21**, 1460 (1980).

[8] V. I. Markushin (private communication, 1989).

[9] R. Frosch, Paul Scherrer Institute, Internal Report No. TM-37-21, 1985 (unpublished).

[10] John B. Czirr, Phys. Rev. **130**, 341 (1963).

[11] R. M. Marshall, Ph.D. thesis, University of Virginia, 1985.

[12] J. F. Crawford, *et al.*, Paul Scherrer Institute, Proposal R-85-10 (unpublished).

[13] F. James and M. Roos, CERN Computer Program Library D507 (1967).

[14] R. Abela *et al.*, Phys. Lett. B **146**, 431 (1984).

[15] M. Daum *et al.*, presented at the XII International Conference on Particles and Nuclei, Cambridge, Massachusetts, 1990 (unpublished).

[16] I. M. Vasilevsky *et al.*, Phys. Lett. **23**, 281 (1966).

[17] J. F. Crawford, *et al.*, Phys. Rev. Lett. **56**, 1043 (1986).

[18] J. F. Crawford *et al.*, Paul Scherrer Institute Nuclear and Particle Physics Newsletter, 1989 (Paul Scherrer Institute, Switzerland, 1990), p. 19.